Journal of the Meteorological Society of Japan, **99**(1), 181−200, 2021. doi:10.2151/jmsj.2021-010 **181**
Special Edition on Global Precipitation Measurement (GPM): 5th Anniversary

Path Attenuation Estimates for the GPM Dual-frequency Precipitation Radar (DPR)

Robert MENEGHINI

NASA Goddard Space Flight Center, Maryland, USA

Hyokyung KIM, Liang LIAO

Morgan State University, Goddard Earth Science Technology Research, Maryland, USA

John KWIATKOWSKI

George Mason University, Goddard Space Flight Center, Maryland, USA

and

Toshio IGUCHI

University of Maryland, Goddard Space Flight Center, College Park, Maryland, USA

(Manuscript received 2 April 2020, in final form 27 October 2020)

Abstract

Estimation of path attenuation is a critical part of retrieving precipitation parameters using measurements from the Dual-frequency Precipitation Radar (DPR) on board the Global Precipitation Measurement Mission (GPM) satellite. In this paper, we describe the latest implementation of the surface reference technique (SRT) that uses surface scattering properties to infer path attenuation through the precipitation. Both single- and dual-frequency versions of this method are available and although the dual-frequency version appears to be more accurate at moderate rain rates, the single-frequency approach at Ku-band is needed when the Ka-band data are not available. Despite improvements afforded by the dual-frequency version of the method, other methods such as the Hitschfeld-Bordan and standard dual-frequency approaches offer advantages particularly at lighter rain rates and at near-nadir incidence angles over land. Weighted averages of the results from these methods appear to offer the best estimate of path attenuation presently available.

Keywords attenuation; radar; surface scattering; Dual-frequency Precipitation Radar; Global Precipitation Measurement Mission

Citation Meneghini, R., H. Kim, L. Liao, J. Kwiatkowski, and T. Iguchi, 2020: Path attenuation estimates for the GPM Dual-frequency Precipitation Radar (DPR). *J. Meteor. Soc. Japan*, **99**, 181–200, doi:10.2151/jmsj.2021-010.

1. Introduction

At microwave frequencies, signals are attenuated by cloud, atmospheric gases, and precipitation. The presence of attenuation implies that accurate estimates of the precipitation at any range depend on how well the radar return signal to and from that range can be cor-

---

Corresponding author: Robert Meneghini, NASA Goddard Space Flight Center, Code 612, 8800 Greenbelt Rd, Greenbelt, Maryland 20771, USA
E-mail: robert.meneghini-1@nasa.gov
J-stage Advance Published Date: 19 November 2020

rected for this effect. The surface reference technique (SRT) has been one of the ways of providing information about the path integrated attenuation (PIA), using the difference in surface returns outside and within the rain (Meneghini et al. 1983, 2000, 2004; Durden et al. 1998, 2003; Li et al. 2002, 2004). The reliability of the method depends on the inherent variability of the surface cross section which changes as a function of the radar frequency, incidence angle, and surface type. With dual-frequency data, the technique can be extended to two frequencies where the differential cross section, the difference between the normalized radar cross section (NRCS) at Ku-band and Ka-band, $\delta\sigma^0 = \sigma^0(Ka) - \sigma^0(Ku)$, can be measured inside and outside the rain to yield an estimate of the differential path attenuation, $\delta A = A(Ka) - A(Ku)$. The high correlation between $\sigma^0(Ku)$ and $\sigma^0(Ka)$ over most surface types and incidence angles implies that the variance of $\delta\sigma^0$ is typically smaller than the variance of $\sigma^0(Ku)$ or $\sigma^0(Ka)$ alone. This greater stability in the reference data yields more accurate estimates of the differential attenuation than the single-frequency estimates of $A(Ku)$ or $A(Ka)$.

Despite improvements in accuracy in moving from single- to dual-frequency data, the SRT remains subject to large relative errors at light rain rates. Moreover, in heavy rain, the Ka-band surface return can be lost so that only the single-frequency Ku-band SRT is available. Another limitation of dual-frequency retrievals stems from the fact that at very light rain rates, only the DPR Ku-band channel detects rain; i.e., the Ku-band channel is more sensitive than the Ka-band. To improve accuracy, we combine the SRT estimates with the well-known Hitschfeld-Bordan (HB) method (Hitschfeld and Bordan 1954). For dual-frequency operation, we also consider the use of the standard dual-frequency attenuation method where a difference in the measured radar reflectivity factors near the surface can be related to the differential path attenuation. The goal is to construct an estimate of path attenuation that uses the best features of the single- and dual-frequency estimates, using both SRT and non-SRT approaches, to provide the most accurate constraint to characterize the precipitation.

As the Ka-band scan pattern on the Japanese Aerospace Exploration Agency's (JAXA) Dual-frequency Precipitation Radar (DPR) was changed in May 2018 so that dual-frequency coverage became available over the full swath, the focus in this paper will be on dual-frequency results. Nevertheless, the single-frequency Ku-band estimates play an important supporting role in cases where the Ka-band data are not available either because of detection limitations at light rain rates or because of signal loss from attenuation at heavier rain rates.

In Section 2 we review the basic equations that describe the operational implementation of the single- and dual-frequency SRT. The same formalism can be used for the single- and dual-frequency hybrid estimates. In Section 3, examples are shown that illustrate strengths and weaknesses of the methods followed by statistical comparisons among the approaches in Section 4. Discussion and summary are given in Section 5.

2. Basic equations for the SRT and hybrid estimates of path attenuation

2.1 Single-frequency estimates

The Hitschfeld-Bordan (Hitschfeld and Bordan 1954) equation provides the attenuation-corrected radar reflectivity factor, Z (mm^6 m^{-3}), along the radar column in terms of the measured radar reflectivity factor, Z_m, and the parameters α, β of a power law k-Z relationship, $k = \alpha Z^\beta$, where k is the specific attenuation in dB km^{-1}. For simplicity, Z and Z_m will be referred to as the true and measured reflectivities, respectively. As an aside, we note that the term "measured" is appropriate in the sense that this quantity can be obtained directly from the radar return power using the standard meteorological radar equation. Letting r be the range from the radar to the center of an arbitrary volume element along the radar beam, the HB solution can be written in the following form (Iguchi and Meneghini 1994):

$$Z(r) = Z_m(r) / [1 - \zeta(r)]^{1/\beta}, \tag{1}$$

$$\zeta(r) = 0.2\beta \ln 10 \int_0^r \alpha(s) Z_m(s) ds. \tag{2}$$

The two-way path attenuation (dB), or what is often termed the path-integrated attenuation, PIA, to range r is defined by

$$A(r) = 2\int_0^r k(s) ds. \tag{3}$$

Where Z, Z_m and A are related by the equation

$$10\log_{10} Z(r) = 10\log_{10} Z_m(r) + A(r). \tag{4}$$

Taking 10 $\log_{10}$ of (1) and using (4) yields the HB estimate of the PIA to range r:

$$A_{HB}(r) = -(10/\beta)\log_{10}[1 - \zeta(r)]. \tag{5}$$

The SRT was originally introduced as a way to constrain solutions to the HB equation, particularly for cases where the PIA is large and (1) tends to become unstable, i.e., $\zeta \rightarrow 1$. For a single frequency radar, the SRT-PIA is given simply by the difference between the surface cross sections, σ^0, in dB, at a rain-free area, σ^0_{NR}, or an average of such measurements, and the surface cross section in the rainy area, σ^0_R, where the PIA is wanted:

$$A_{SRT}(r_s) = \sigma^0_{NR} - \sigma^0_R, \tag{6}$$

where r_s is the radar range to the surface and where both measurements are taken over the same surface type, frequency and incidence angle. Since the objective is to extract information about the precipitation, the rain-free reference should be taken either close to the raining area or, at a different time, under rain-free conditions, at the same location to minimize the change in the intrinsic surface cross section. The choice of rain-free reference is discussed below.

Comparison of (5) and (6) shows that the two PIA estimates can be directly compared if, in (5), r is set to r_s. This, however, is not possible since Z_m is measurable only up to the last surface clutter-free range gate. In practice, extrapolation is needed to extend Z_m from range r to r_s. The extent of the surface clutter depends on the incidence angle and the relative strengths of the returns from the surface and precipitation. These issues will be discussed later in the paper.

In practice, there are several different ways to estimate the rain-free reference NRCS. An obvious choice is to average the rain-free data at each incidence angle just before rain is encountered. An alternative is to fit the cross-track variations of the rain-free cross sections to a fitting function such as a quadratic. These forward along-track (FA) and forward cross-track (FX) estimates can be repeated by processing the orbit backward (BA, BX) so that the rain-free data are taken after rather than before rain is detected. A fifth type of reference is obtained from the sample mean and standard deviation of the rain-free NRCS at each incidence angle and at each cell within a latitude-longitude grid. As the cross-track fitting approach works well over ocean but not over land because of the high variability of the surface cross section at near-nadir angles, there are five estimates of the SRT-PIA over ocean and three over land. To combine these estimates into a single PIA estimate, we make use of the fact that if the resultant estimate is written as a weighted combination of the individual estimates, then the minimum variance of the combined estimate is obtained by taking the weights to be proportional to the inverse variance of the estimate. In equation form, this can be written

$$A_{SRT} = \sum_{i=1}^{n} w_i A_i, \tag{7}$$

$$w_i = u_i \Big/ \sum_{i=1}^{n} u_i; \quad u_i = 1/\mathrm{var}(A_i), \tag{8}$$

where n is either 3 or 5. Versions of (7) occur frequently in the literature and can be derived by the method of Lagrange multipliers (e.g., Daley 1991). Since the individual PIA estimates are independent, the variance of A_{SRT} is the sum of the variances of $(w_i A_i)$ which can be simplified to:

$$\mathrm{var}(A_{SRT}) = \left\{ \sum_{i=1}^{n} [\mathrm{var}(A_i)]^{-1} \right\}^{-1}, \tag{9}$$

where A_1 and A_2 are associated with the forward and backward along-track estimates, A_3 and A_4 with the forward/backward cross-track estimates and A_5 with the temporal, e.g.,

$$A_1 = A_{SRT}(FA, r_s) = \sigma^0_{NR}(FA) - \sigma^0_R, \tag{10}$$

$$A_2 = A_{SRT}(BA, r_s) = \sigma^0_{NR}(BA) - \sigma^0_R. \tag{11}$$

Similar definitions apply to the cross-track (FX/BX) and temporal estimates. To explore in more detail how the temporal estimate is formed, consider a measurement of the normalized surface cross section in rain, σ^0_R, at incidence angle θ_i that falls within a particular latitude-longitude cell [lat(j), lon(k)]. The temporal estimate of the PIA is obtained by subtracting σ^0_R from the mean rain-free NRCS taken from the look-up table, derived from prior measurements at the (i, j, k) cell with a weighting factor inversely proportional to the sample variance of rain-free data stored at this (i, j, k) entry. The reference data are considered valid only if the number of data samples that comprise the sample statistics at this cell exceeds some threshold (typically 20). Similar remarks apply to the forward along-track reference data where the sample mean and variance at angle θ_i are obtained from the eight rain-free NRCS data points at angle θ_i taken before the field of view containing rain at the same incidence angle. The cross-track estimates of mean and variance are done somewhat differently. For this case, two quadratic fits are done, one over data from the inner swath (inner 25 angle bins, 13–37) and a second on data in the outer swath (angle bins 1–12 and 38–49) where the value of σ^0_{NR} at each angle bin is taken to be the average of the last 8 rain-free NRCS values. The separate fits over the inner and outer swaths are done to mitigate the deviations of the actual data from quadratic behavior over the full swath (Seto and Iguchi 2007). Quadratic fits through these data yield an estimate of $\sigma^0_{NR}(\mathrm{FX})$ for the forward processed data at each incidence angle with a variance taken to be the chi-squared error of the fit. Similar remarks apply to the backward cross-track reference data, $\sigma^0_{NR}(\mathrm{BX})$.

Finally, it is important to note in (9), that the variance of the ith estimate is given by the sum of the variances of the rain-free reference data and the variance of the NRCS in rain. For the first term, we use the sample variance of the rain-free reference data as described above. For the variance of the NRCS in rain, the standard expression for the variance of a Rayleigh target is used, where, for a logarithmic receiver, the variance is given by $(5.57^2/N)$ dB where N is the number of independent samples ($N \sim 100$) at each field of view. For the dual-frequency SRT, the sampling error variance is twice this value. For the results given in this paper, we neglect the error variances arising from the finite number of samples. This issue is discussed further in Section 4.

2.2 *Dual-frequency estimates*

The equations above apply to either the Ku-band or the Ka-band data. The dual-frequency analog of the SRT can be obtained by using (6) and simply subtracting the Ku-band estimate from the Ka-band estimate (Tanelli et al. 2006; Meneghini et al. 2012, 2015). Using the notation δx to indicate the difference in x between its value at Ka-band and Ku-band, i.e., $\delta x = x(Ka) - x(Ku)$, yields:

$$\delta A = \delta\sigma^0_{NR} - \delta\sigma^0_{R}, \tag{12}$$

$$\delta A \equiv A(Ka) - A(Ku). \tag{13}$$

Note that (13) is simply the definition of δA whereas (12) provides an estimate of this quantity using measurements of the NRCS at both frequencies inside and outside the raining area. The analogs to (7)–(9) are:

$$\delta A_{SRT} = \sum_{i=1}^{n} v_i \delta A_i, \tag{14}$$

$$v_i = u_i \Big/ \sum_{i=1}^{n} u_i; \quad u_i = 1/\mathrm{var}(\delta A_i), \tag{15}$$

$$\mathrm{var}(\delta A_{SRT}) = \left\{ \sum_{i=1}^{n} [\mathrm{var}(\delta A_i)]^{-1} \right\}^{-1}. \tag{16}$$

The interpretation of (14)–(16) is similar to the previous equations with $\delta\sigma^0$ replacing σ^0 and with the requirement that $\delta\sigma^0$ be measured at approximately the same location, time and incidence angle.

To compare estimates from (7) and (14), it is necessary to convert δA to $A(Ku)$ or $A(Ka)$ or conversely. One way to do this is simply to assume that the ratio $A(Ka)/A(Ku)$ is constant. This ratio can be computed by the use of raindrop size distributions taken along a simulated radar path from which $A(Ku)$, $A(Ka)$ and δA can be computed for each realization. These numerical experiments suggest that a value of 6 for the $A(Ka)/A(Ku)$ ratio is a reasonable assumption (Meneghini et al. 2012). Nevertheless, the fluctuations about the $A(Ku)$ versus $A(Ka)$ linear regression line show that errors will arise in any conversion between δA and $A(Ku)$ or $A(Ka)$. In this paper we will ignore these conversion errors because in the solver module (Seto et al. 2013, 2016, 2020; Seto and Iguchi 2015) δA is used as a constraint for the dual-frequency rain retrieval whereas $A(Ku)$ [or $A(Ka)$] is used as a constraint in the single-frequency retrieval. This implies that we can assess the errors in δA and $A(Ku)$ or $A(Ka)$ without converting from one to the other. However, for dual-frequency retrieval algorithms that require both $A(Ku)$ and $A(Ka)$, rather than simply δA, the conversion error made in going from δA to $A(Ku)$ and $A(Ka)$ becomes relevant and must be included in the error modeling (Meneghini et al. 2012).

As noted earlier, the advantage of the dual-frequency formulation is that the variance of $\delta\sigma^0$ tends to be smaller and more uniform, both spatially and with incidence angle, than the variance of either $\sigma^0(Ku)$ or $\sigma^0(Ka)$. These features can be seen in Fig. 1 that show the standard deviation of $\sigma^0(Ku)$, $\sigma^0(Ka)$, and $\delta\sigma^0$ over ocean and land using DPR data from September to November 2018. As noted earlier, the Ka-band scan pattern was changed on 21 May 2018 so that nearly simultaneous, matched-beam data are available for both frequencies for incidence angles from 0^0 to 18^0.

The results of Fig. 1 show that the standard deviation, SD, in dB, of $\sigma^0(Ku)$ and $\sigma^0(Ka)$ over ocean changes significantly with incidence angle, with minima near 5^0 and attaining maximum values at 18^0, where $\mathrm{SD}[\sigma^0(Ku, 18^0)] \approx 3.4$ dB and $\mathrm{SD}[\sigma^0(Ka, 18^0)] \approx 3.7$ dB. In contrast, $\delta\sigma^0$ is approximately constant with angle with an SD near 1 dB. Over land, the SD of $\delta\sigma^0$ decreases rapidly over the first three angle bins (0^0 to 1.5^0), followed by a slower decrease at higher angles and finally becoming asymptotic to a value of about 1 dB at 18^0. The SDs of $\sigma^0(Ku)$ and $\sigma^0(Ka)$ over land show similar rapid and slower decreases with

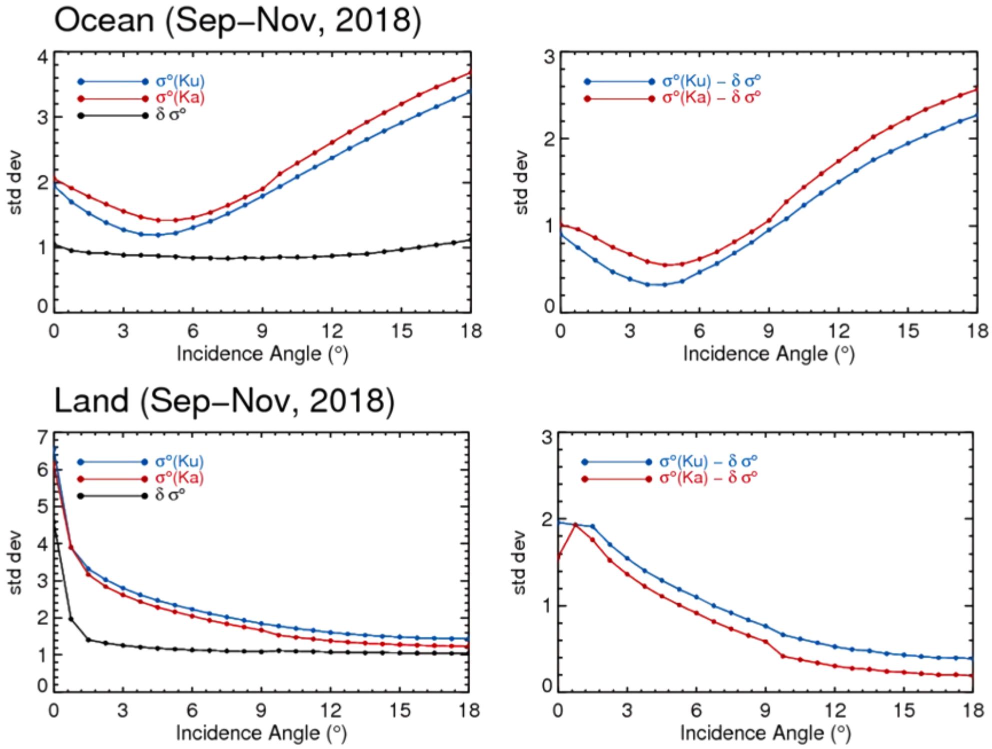

Fig. 1. Top left: Standard deviations of $\sigma^0(Ku)$, $\sigma^0(Ka)$, and $\delta\sigma^0$ versus incidence angle over ocean; Top right: differences in standard deviations between $\sigma^0(Ku)$ and $\delta\sigma^0$ and between $\sigma^0(Ka)$ and $\delta\sigma^0$. Bottom left: Standard deviations of $\sigma^0(Ku)$, $\sigma^0(Ka)$, and $\delta\sigma^0$ versus incidence angle over land; Bottom right: differences in standard deviations between single-frequency NRCS and $\delta\sigma^0$. Data were measured during September-November, 2018.

increasing angle from nadir; the SDs, however, especially at near-nadir angles, are significantly larger than that of $\delta\sigma^0$. Differences in SD between $\sigma^0(Ku)$ and $\delta\sigma^0$ and between $\sigma^0(Ka)$ and $\delta\sigma$ as a function of angle are shown in the top and bottom, right-hand panels. This reduction in the SD in going from single- to dual-frequency results is critical in determining the efficacy of the SRT, particularly at light rain rates where the SD can be comparable to or greater than the path attenuation itself. It is worth noting here that, unlike errors in the non-SRT methods discussed below, the errors in the SRT are independent of the magnitude of the path attenuation as long as the surface return(s) are detectable.

Using the same September-November 2018 data set, the spatial distributions of SD for $\sigma^0(Ku)$ (top), $\sigma^0(Ka)$ (center) and $\delta\sigma^0$ (bottom) are shown in Fig. 2 for an incidence angle of 9^0. Note the lower values and greater spatial homogeneity in the SD of $\delta\sigma^0$ compared with those of $\sigma^0(Ku)$ and $\sigma^0(Ka)$. At incidence angles greater than 9^0, the difference between the SDs of $\delta\sigma^0$ and σ^0 increases over ocean but lessens over land. At near-nadir angles, the effects are reversed, where greater differences in the SD between $\delta\sigma^0$ and σ^0 occur over land and smaller differences over ocean.

2.3 Hybrid estimates

As the SRT, HB, and standard dual-wavelength methods (DW) (Durden 2018; Meneghini et al. 1992; Eccles and Mueller 1971) are mutually independent, the same formalism can be used to combine them. For single-frequency applications, the DW is unavailable so we are left with only the HB and SRT to generate a hybrid path attenuation, A_{HY}, for either Ku- or Ka-band data:

$$A_{HY} = w_{SRT} A_{SRT} + w_{HB} A_{HB}. \tag{17}$$

As before, the weighting factors are inversely proportional to the variance of the estimate so that $w_{HB} \sim 1/\mathrm{var}(A_{HB})$ and where A_{SRT} and w_{SRT} are given by (7) and (9) respectively.

Note that single- and dual-frequency hybrid methods are analyzed separately in this paper and not combined into a generic hybrid estimate that covers

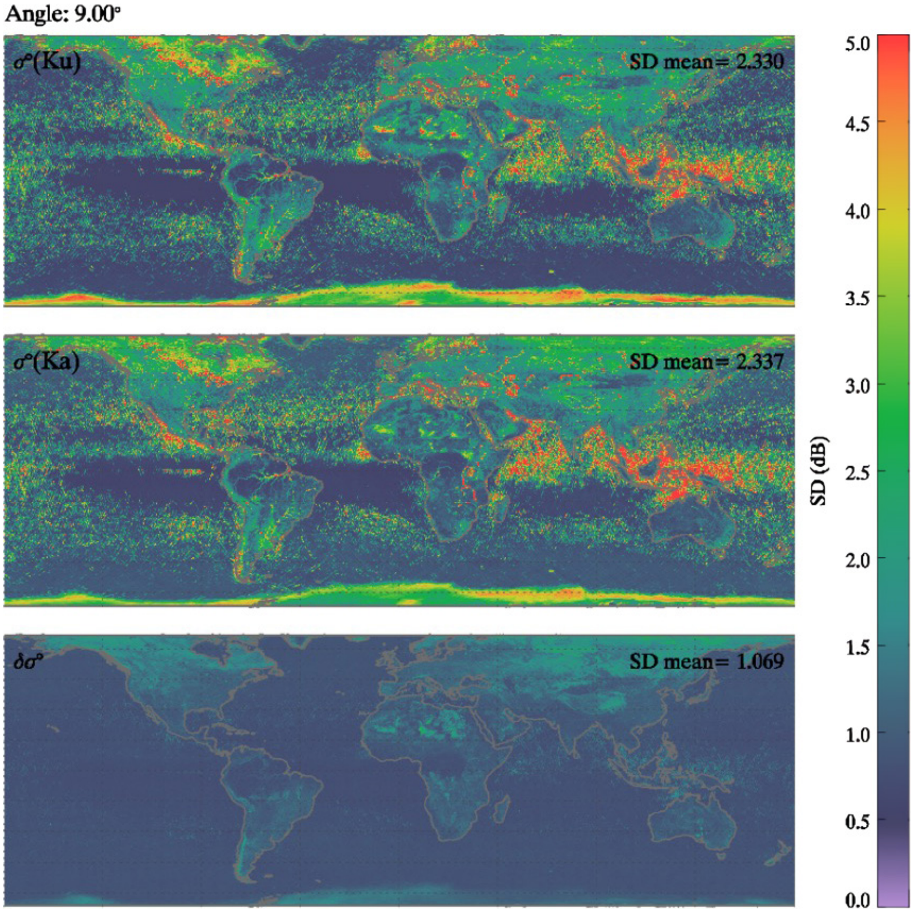

Fig. 2. Maps of the sample standard deviation of the NRCS at an incidence angle of 9^0, computed over a latitude/longitude grid of 0.5^0 for $\sigma^0(Ku)$ (top), $\sigma^0(Ka)$ (center) and $\delta\sigma^0$ (bottom) from DPR data acquired during September-November 2018.

all cases. One of the reasons for this separation is that in the operational system, the Ku-band and Ka-band data are processed individually before the data are combined for dual-frequency processing. As a consequence, dual-frequency information is unavailable for single-frequency analysis. In Section 5 we briefly discuss the possibility of combining single- and dual-frequency hybrid estimates.

For the differential path attenuation, the DW, δA_{DW}, can be added so that

$$\delta A_{HY} = v_{SRT}\delta A_{SRT} + v_{HB}\delta A_{HB} + v_{DW}\delta A_{DW}, \tag{18}$$

$$\begin{aligned} &v_{SRT} = 1/[k\,\mathrm{var}(\delta A_{SRT})]; \quad v_{HB} = 1/[k\,\mathrm{var}(\delta A_{HB})]; \\ &v_{DW} = 1/[k\,\mathrm{var}(\delta A_{DW})] \\ &k = 1/\mathrm{var}(\delta A_{SRT}) + 1/\mathrm{var}(\delta A_{HB}) + 1/\mathrm{var}(\delta A_{DW}). \end{aligned} \tag{19}$$

An estimate for δA_{DW} can be obtained from the relationship $\delta A = DFR_m - DFR$, where $DFR_m = 10\log_{10}[Z_m(Ku, r_{ns})/Z_m(Ka, r_{ns})]$, $DFR = 10\log_{10}[Z(Ku, r_{ns})/Z(Ka, r_{ns})]$, where r_{ns} indicates the radar range to the near-surface gate where the precipitation return is much larger than the surface return. As the PIA is combined with that from the SRT, which gives the path attenuation to the surface, the goal is to evaluate the DFR_m as close to the surface as possible or to extrapolate the Z_m values to the surface. A shortcoming of this expression for δA is that while DFR_m is measurable, DFR is not. One approximation is simply to ignore DFR by noting that for raindrop particle size distributions with a mass-weighted drop diameter, D_m, of less than approximately 1.5 mm the error typically will be less than ± 1 dB. Another approximation is to use $Z_m(Ku)$ (in dB) near the surface to estimate DFR.

In this case, δA_{DW}, can be written:

$$\delta A_{DW} = DFR_m - DFR[Z_m(Ku)]. \tag{20}$$

To compute the mean and variance of the second term of (20), we use measured raindrop size distributions, RSDs, obtained from several NASA field campaigns (Liao and Meneghini 2019). Sequences of these are used to simulate the variability along a column of rain; for example, for a 4 km path with a range gate spacing of 0.125 km, 32 RSDs are used to construct the path. Note that the correlation in rain rate and the median mass diameter along the column, generated from the RSDs, generally conforms to the results from a combined study of Micro Rain Radar (MRR) and RSD measurements reported by Adirosi et al. (2016). From these data, beginning from the top down, $Z(f, r)$ and $Z_m(f, r)$, for $f = 13.6$ GHz, and $f = 35.5$ GHz, are computed at each range, r, along the column so that DFR and $Z_m(Ku)$ are available at the bottom-most range of the column. Repeating this procedure for ~ 28,000 such simulated rain columns provides 2-D histograms of DFR versus $Z_m(Ku)$ as shown in the top panels of Fig. 3 for rain path lengths of 4 km and 5 km. The plots just below these (center) summarize the data by plotting the mean (blue lines) along with third-order polynomial fits of the mean given by the red lines. The vertical blue lines extend one standard deviation above and below the mean curve. These standard deviations are displayed in the bottom plots (blue lines) along with third-order polynomial fits (red lines).

The results on the bottom panels of Fig. 3 represent the standard deviation of the second term in (20). The error variance in the first term in (20) arises from the sampling errors, caused by the finite number of independent samples, used in computing DFR_m. As the Z_m data are derived from N independent samples from a logarithmic receiver (where $N \sim 100$) the variance is given by $2 \times (5.57)^2/N$, where the factor of 2 arises from the fact that the Ku- and Ka-band statistics are identical and independent. Since the variance from RSD fluctuations and from finite sampling are independent, the variances add so that the modified SD is given by the square root of the sum of the two variances. As noted earlier, similar considerations apply to the SRT.

These simulated rain columns can also be used to characterize the standard deviation, SD, in the HB estimates. In Fig. 4, top, plots of SD for Ku, Ka and (Ka-Ku) path attenuations are shown as a function of ζ for a path length of 4 km along with best-fit cubic polynomials. It should be noted that for the SD plot of Ku, the quantity plotted along the x-axis is $\zeta(Ku)$ whereas for the SD of Ka and Ka-Ku, the x-axis variable should be interpreted as $\zeta(Ka)$.

Note that the best-fit α, β values for Ku, Ka and Ka-Ku were obtained from the full set of RSDs using a linear regression in log space ($\log k = \log \alpha + \beta \log Z$, $\log \delta k = \log \alpha' + \beta' \log \delta Z$). Shown in Fig. 4 (bottom) is a scatter plot of $\zeta(Ka)$ versus $\zeta(Ku)$ illustrating that the $\zeta(Ku)$ values tend to be concentrated at small values (low attenuation) where the standard deviation of the estimate is small. In contrast, the $\zeta(Ka)$ values are significantly higher with slightly over 8 % of the profiles yielding $\zeta(Ka) > 1$ where the HB equation fails to produce a meaningful estimate. Note that the δA_{HB} estimate is simply obtained by forming the difference $A_{HB}(Ka) - A_{HB}(Ku)$. As such, it is not a differential attenuation estimate in the same sense as δA_{SRT} or δA_{DW} which are derived directly from measured data without first computing the path attenuations at Ku and Ka-band. Moreover, as shown in Fig. 4 (top), the error in δA_{HB} is dominated by the error in $A_{HB}(Ka)$. In contrast, the SRT error variance generally decreases in going from single to dual-frequency implementation as shown by the standard deviations in Fig. 1. These characteristics imply that in the hybrid estimate of δA, the SRT is expected to dominate for moderate-heavy rain rates as the error variance will tend to be smaller than those of either HB or DW. In contrast, for a single-frequency Ku-band estimate, where the error variance for SRT can be substantial, particularly over ocean at off-nadir incidence and near-nadir incidence over land (Fig. 1), we expect a reversal where the HB will tend to be more highly weighted than the SRT, particularly at light rain rates (low attenuations) where the HB standard deviation at Ku-band tends to be small.

Table 1 provides a qualitative idea of the weightings of the different methods as a function of background type, frequency and rain rate. Categories 1–3 over ocean are defined as low, moderate and heavy rain rates, respectively. Categories over land are defined as follows: category 1' comprises cases of either low rain rate or near-nadir incidence, category 2' comprises cases of moderate rain rate and off-nadir incidence, category 3' comprises cases of high rain rate and off-nadir incidence. Note that the actual weights of the methods are proportional to the inverse of the variance, which, as discussed above, vary continuously with rain rate and, for the SRT, with incidence angle.

Before moving to the experimental results, two further remarks should be made. Unlike the DW or SRT

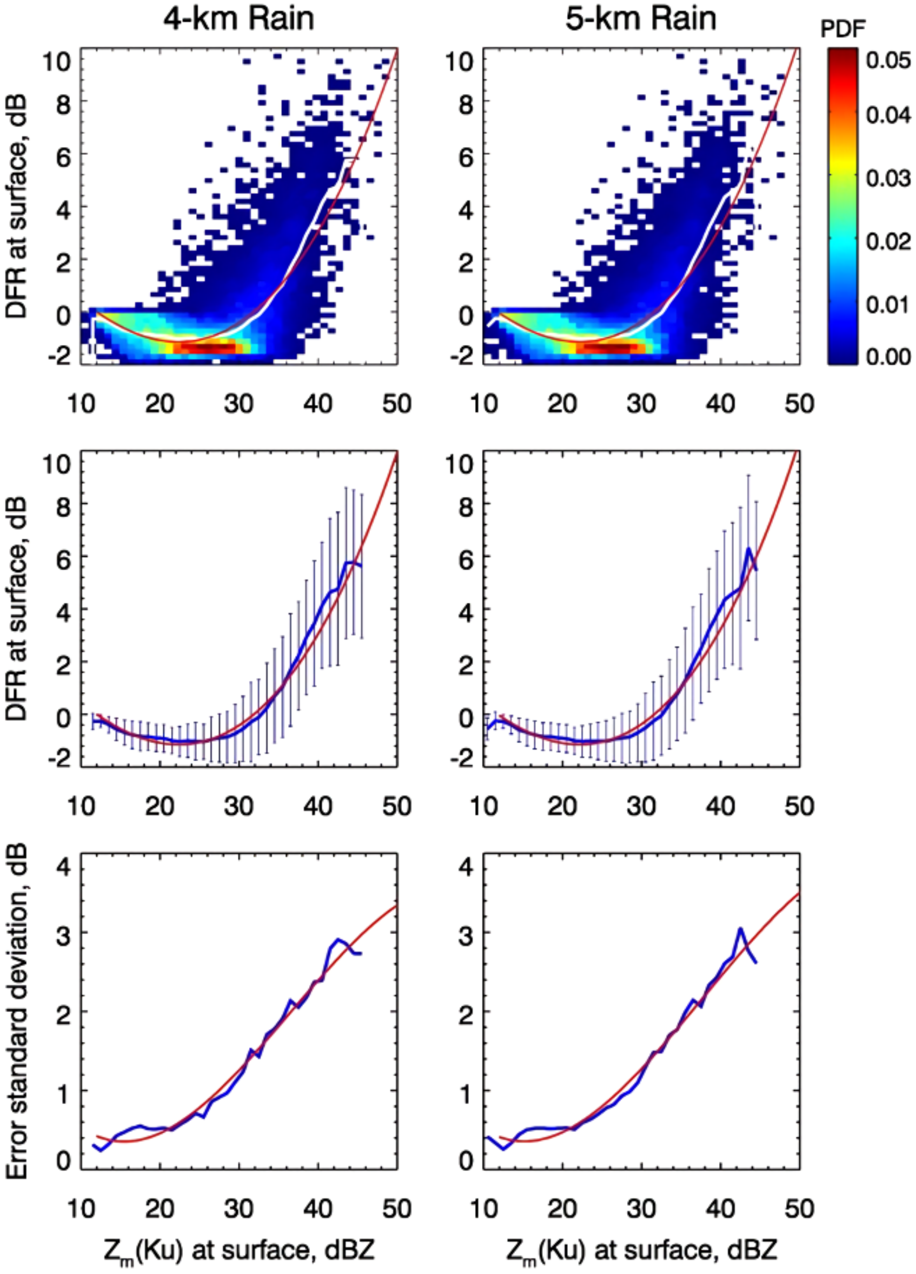

Fig. 3. Top: Simulated 2D histograms of DFR versus $Z_m(Ku)$ at the surface for rain path lengths of 4 km and 5 km. Center: Mean DFR versus $Z_m(Ku)$ (blue line) along with a cubic polynomial fit (red line) as derived from the data in the top panels. The vertical blue lines extend one standard deviation above and below the mean. Bottom: Standard deviation of DFR[$Z_m(Ku)$] versus $Z_m(Ku)$ for path lengths of 4 km (left) and 5 km (right) are shown by the blue lines; cubic polynomial fits are given by the red lines.

methods, where sampling errors can be significant, for the HB, the sampling errors in Z_m, enter into the estimate via (2) and (5). Since these errors are independent and identically distributed from gate to gate, the fluctuations decrease when they are summed over the path. The second point that should be made is on the similarities between the hybrid estimate given by (17) and those obtained by Iguchi et al. (2000, 2009). It can

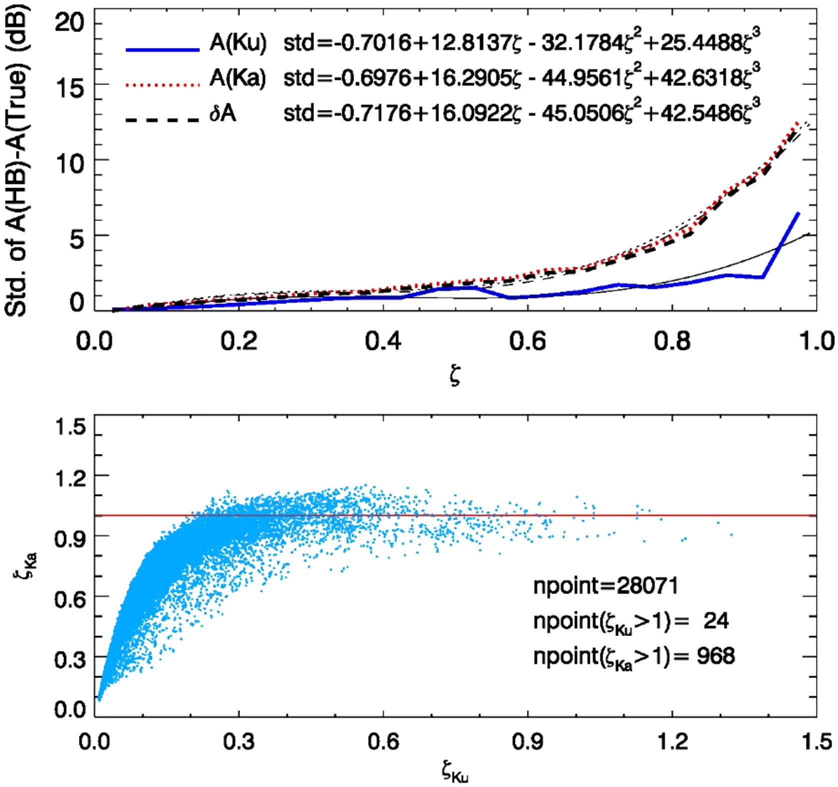

Fig. 4. Top: Standard deviations of A_{HB}, relative to the true path attenuation, as a function of ζ for Ku, Ka, and (Ka-Ku). Note that for the Ku-band results, the *x*-axis represents $\zeta(Ku)$ while for the Ka-band and differential results, the *x*-axis represents $\zeta(Ka)$. Cubic fits for the SD versus ζ for $A_{HB}(Ku)$, $A_{HB}(Ka)$, and δA_{HB} are shown in the inset. Bottom: Scatter plot of $\zeta(Ka)$ versus $\zeta(Ku)$ for the profiles used in the simulation.

Table 1. Approximate relative weights of methods used in the hybrid estimates.

	Ocean (cat 1)	Ocean (cat 2)	Ocean (cat 3)	Land (cat 1’)	Land (cat 2’)	Land (cat 3’)
$HB(Ku)$	high	moderate	moderate	high	moderate	moderate
$HB(Ka)$	moderate	moderate	low	moderate	moderate	low
δHB	moderate	moderate	low	moderate	moderate	low
$SRT(Ku)$	moderate	moderate	high	low	moderate	high
$SRT(Ka)$	high	high	moderate	moderate	high	moderate
δSRT	high	high	moderate	moderate	high	moderate
DW	moderate	moderate	low	moderate	moderate	low

be shown that the maximum likelihood approach in these papers and the minimum variance approach here are identical if the components, i.e., the various PIA’s, can be modeled as independent, Gaussian random variables. Despite this equivalence, note that in Iguchi et al. (2000, 2009), a critical factor is the behavior of ζ. Following Iguchi et al. (2000) and using the notation given here, the following equation is minimized:

$$D \equiv (A - A_{SRT})^2 / 2\sigma_{SRT}^2 + \{\ln\zeta - \ln[1 - \exp(-0.1\beta A \ln 10)]\}^2 / 2\sigma_{\ln\zeta}^2 , \tag{21}$$

where $\sigma_{\ln\zeta}^2$ is the variance associated with $\ln\zeta$, where ζ is defined by (2). Taking the derivative of D with respect to the Hitschfeld-Bordan PIA estimate, A, and setting the result to zero yields a transcendental equation for A as a function of the mean and variance of A_{SRT} and the mean and variance of $\ln\zeta$. Using the single-frequency SRT/HB combination, comparisons of the hybrid pia obtained from the maximum likelihood methodology, given by minimizing (21), and the minimum variance approach (17), show the results to be quite similar. Nevertheless, specification of the statistics of ζ in the maximum likelihood approach and the need to numerically solve the equation for A_{HB}, instead of directly specifying the statistics of A_{HB} in the minimum variance approach, imply that the two methodologies, at least computationally, are not identical.

3. Examples

Before discussing examples of path attenuation estimates, it is worth recalling that the Ku-band channel of the DPR provides 49 fields of view (FOV) in the cross-track direction with a nadir FOV of approximately 5 km and a swath of 245 km. As the original 24 interleaved Ka-band FOV were redirected on 21 May 2018 to the outer edges of the Ka-band inner swath (25 FOVs), the Ku- and Ka-band data are now approximately matched in space and time over the full swath. This was an important change in several respects; for the SRT and path attenuation estimates generally, the new data should provide insight into how the single- and dual-frequency methods compare at off-nadir angles and whether the use of dual-frequencies offers better constraints for the rain retrievals.

The data shown in Fig. 5 were derived from DPR measurements off Western Australia during orbit 24626 on 30 June 2018. Note that these are dual-frequency estimates over the full swath. To facilitate later comparisons to the Ku-band only data, we have plotted not δA but the Ku-band path attenuation, $A_\delta(Ku)$, where $A_\delta(Ku)$ is derived from δA by assuming that the ratio of Ka-band to Ku-band path attenuation is 6, i.e., $A_\delta(Ku) = 0.2\delta A$. This translation to Ku-band is useful when comparing the dual- and single-frequency results, as will be done later. The notation $A_\delta(Ku)$ will be used to distinguish the dual-frequency estimate from the single-frequency estimate of Ku-band path attenuation which will be denoted simply by $A(Ku)$. The labeling in each panel of Fig. 5 identifies the different products used to obtain the weighted mean shown in the bottom-right panel. Since this example is taken over ocean, five such estimates exist where each has an associated field of weights (not shown) that are used to compute the weighted mean shown in the bottom right-most plot. For the temporal estimate, the rain-free reference data were taken from a lookup table that contains the means, standard deviations and counts for $\sigma^0(Ku)$, $\sigma^0(Ka)$ and $\delta\sigma^0$ over a fixed (latitude, longitude) grid of 0.5^0 for angles from 0^0 to 18^0. As the angle bin increment is approximately 0.75^0, the total number of angle bins is 25. Currently, the signed angle of incidence is not used, and only the magnitude of the incidence angle with respect to nadir is needed in the look-up table.

To form the dual-frequency hybrid estimate, we begin with the weighted SRT result in the bottom-right panel of Fig. 5 along with the associated error variance given by (16), where $\mathrm{var}[A_\delta(Ku)] = 0.2^2\mathrm{var}(\delta A)$. This gives the first term of (18). The second and third terms correspond to the dual-frequency HB and standard dual-frequency (DW) results multiplied by their respective weights. As noted earlier, these weights are inversely proportional to the variance of their respective estimates where the variances for HB and DW were described in the previous section. The results for the SRT, HB, DW and the resultant hybrid path attenuation estimates are shown in Fig. 6. As in Fig. 5, we have converted all δA values to $A_\delta(Ku)$.

To obtain some measure of the goodness of the estimate, a "reliability factor", RF is defined as the ratio of the mean to the standard deviation of the estimate, $\mathrm{RF} = \mathrm{E}(A)/\sigma(A)$. To further simplify the comparison, we define a reliability flag, RFlag, such that when $\mathrm{RF} > 3$, we set RFlag to 1 (reliable, blue), when $1 \leq \mathrm{RF} < 3$, $\mathrm{RFlag} = 2$ (marginally reliable, green) and when $\mathrm{RF} < 1$, $\mathrm{RFlag} = 3$ (unreliable, red). A comparison of RFlag for the SRT and the hybrid estimates is shown in Fig. 7.

Comparisons of the reliability flags for SRT and hybrid show that the hybrid provides more robust estimates, particularly in the light to moderate rain rate/path attenuation areas by supplementing the SRT with the HB and DW estimates. As indicated on the color scale, a small fraction (< 1 %) of the pixels have the reliability flag set to 4; in fact, there is only a single pixel in the far top left of each plot where the flag has been set to 4. (As in Fig. 9 below, this is represented by a deep red color and should be distinguished from the red-orange regions where the estimates are judged to be unreliable where the flag is set to 3.) This value is used to indicate a situation where the surface return at Ka-band is less than 2 dB greater than the receiver noise level. In these areas, SRT(Ka) and DSRT are not strictly applicable since the estimates will generally give a negatively biased estimate of path attenuation. In particular, the estimated $\sigma^0(Ka)$ in rain will be larger than the true value as the surface cross section will be determined by the noise power rather than by

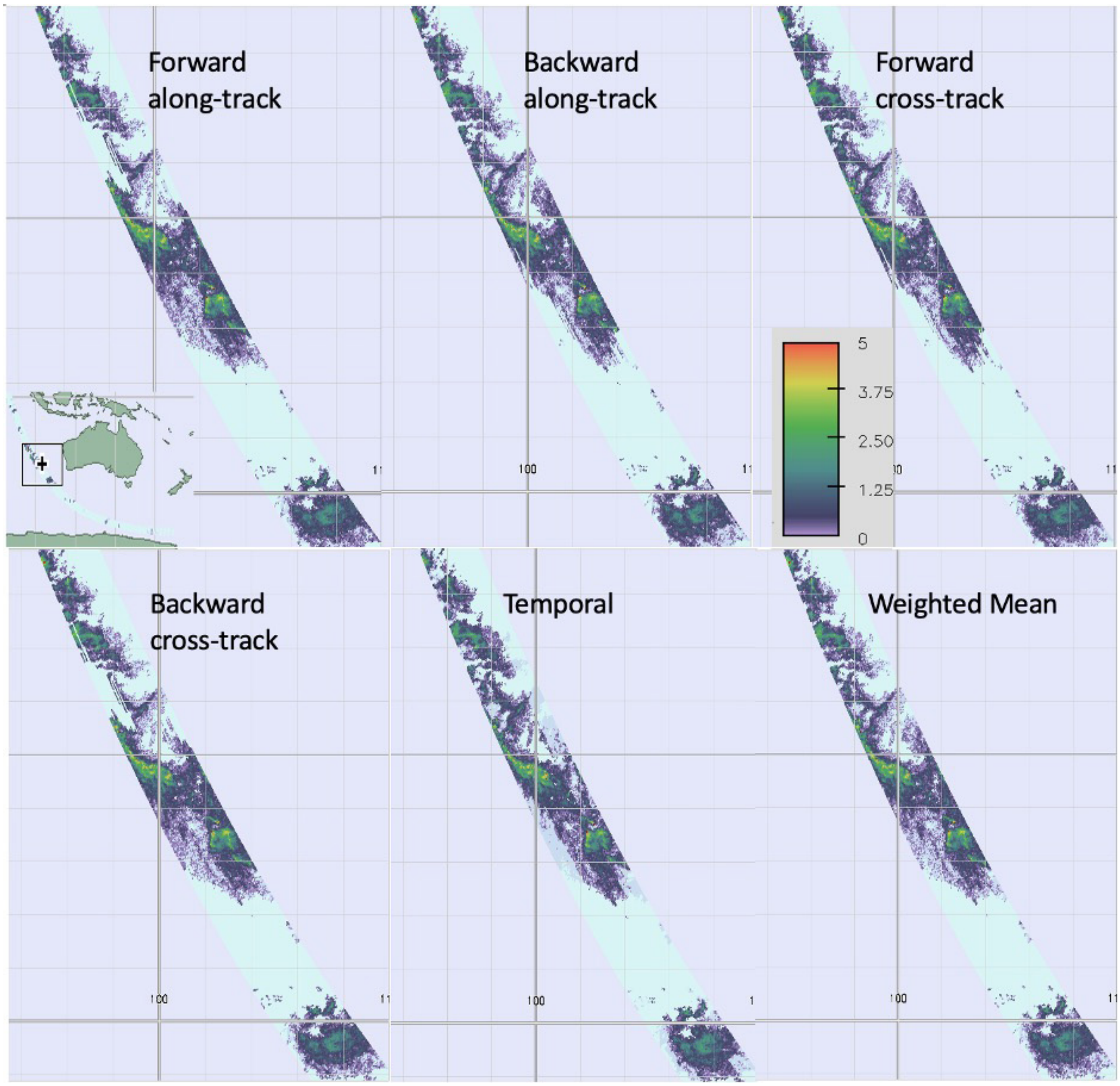

Fig. 5. Ku-band path attenuation estimates in dB derived from the dual-frequency SRT from a section of orbit 24,642 measured over ocean, west of Australia, on 30 June 2018.

the smaller surface return power. In fact, if the surface return is close to the noise level, it follows in almost all cases that the Ka-band rain return near the surface will also be at or below the receiver noise level so that all dual-frequency estimates are suspect. In these cases, the precipitation characteristics, particularly those estimates related to the full path or near the surface, should be estimated solely with the Ku-band data.

Before discussing this problem in more detail, it is worth showing an example of results before and after the change in processing the outer-swath Ka-band data. The left panel of Fig. 8 shows the SRT results before the coding changes where dual-frequency data are processed only in the inner swath, with Ku-band results shown in the outer swath. On the right, the dual-frequency data are processed over the full swath. The image on the right tends to be smoother and less noisy in the outer segments of the swath than the image of the left. Moreover, the result on

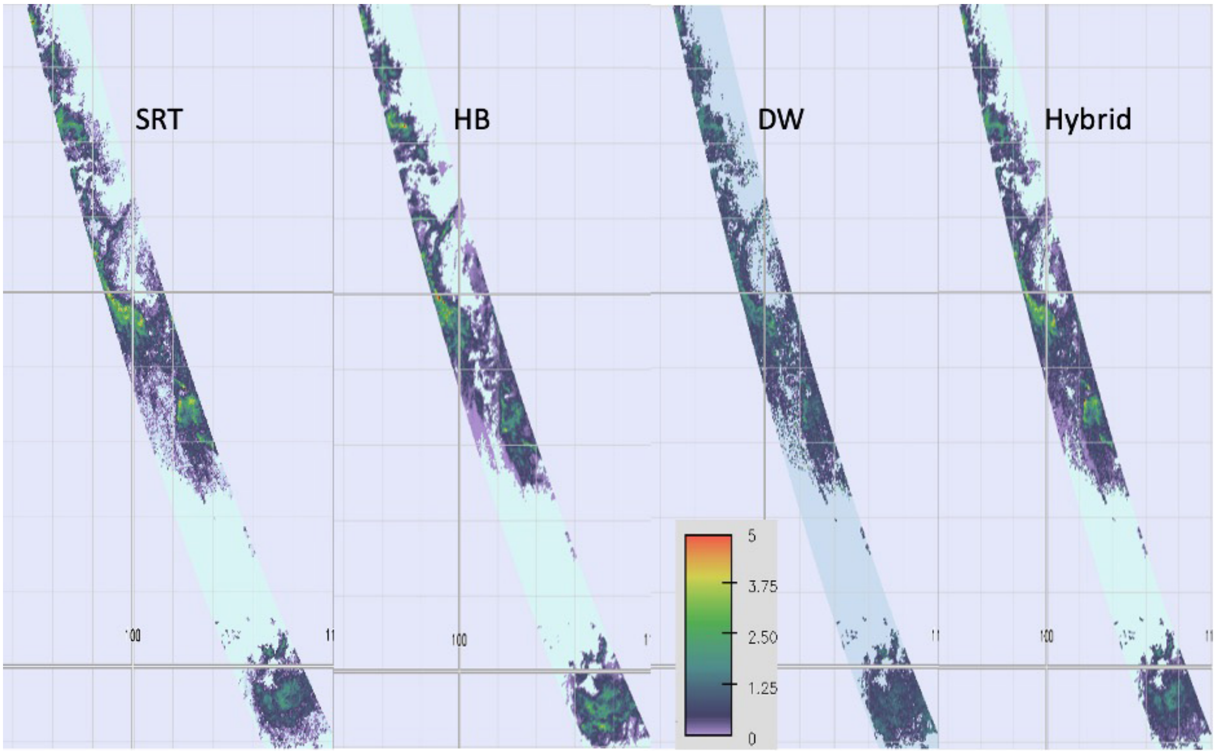

Fig. 6. Ku-band path attenuation estimates in dB derived from the dual-frequency data where the hybrid (far-right panel) PIA is computed as a weighted sum of the PIAs shown in the first three panels. As in Fig. 5, the data were obtained from a segment of orbit 24,642 measured over ocean, off Western Australia, on 30 June 2018.

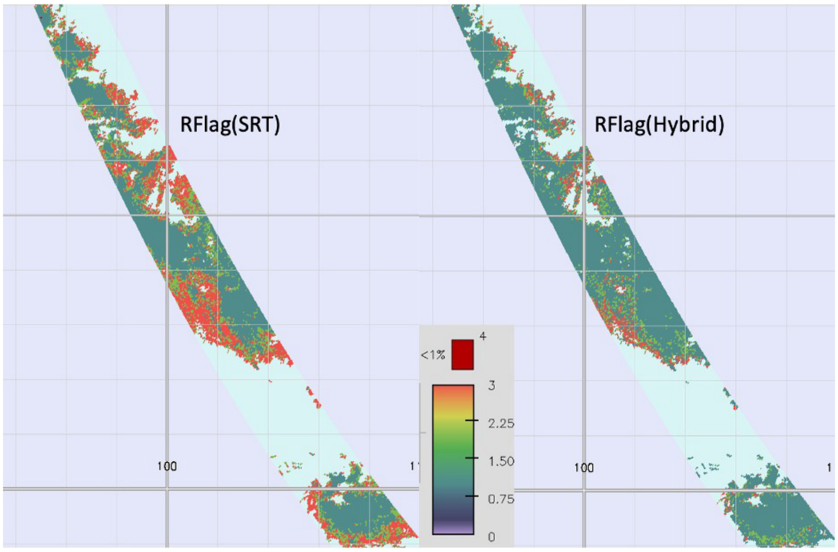

Fig. 7. Reliability flags for SRT (left) and hybrid (right) for the case shown in Fig. 6. Regions of blue define areas where the estimate of path attenuation is considered reliable while regions in red-orange define locations where the estimate is judged to be unreliable. Areas in green indicate locations where the estimate is judged to be marginally reliable.

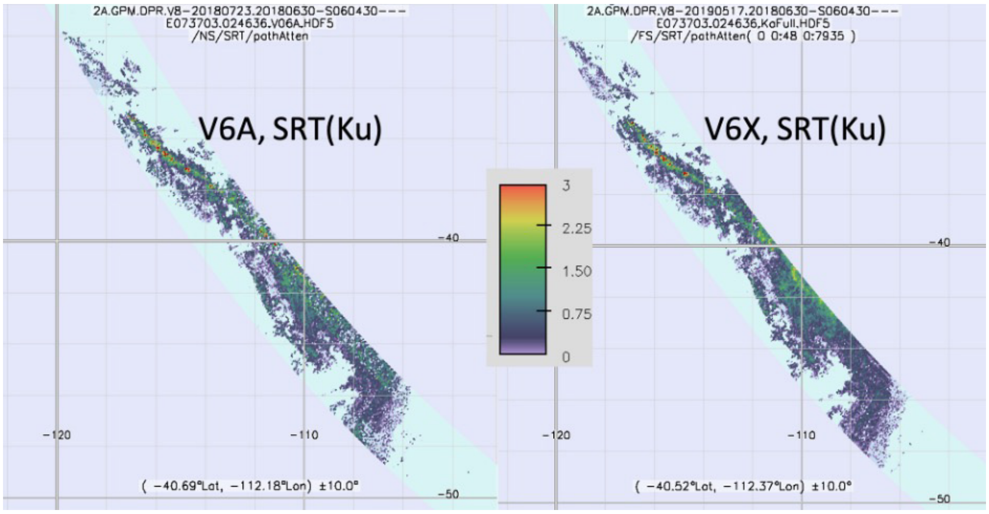

Fig. 8. Path attenuations (dB) from orbit 24,636 (30 June 2018) in the Southwestern Pacific showing the dual-frequency SRT estimate of Ku-band path attenuation. Left: Version V6A where dual-frequency data are used only in the inner swath; Right: Version V6X where dual-frequency data are used over the full swath.

the left shows some discontinuities in crossing from the inner to outer swath, although it should be noted that this problem can also arise from the conversion of δA to $A_\delta(Ku)$ where we have assumed $A_\delta(Ku) = 0.2\delta A$ whereas the true conversion depends on the raindrop size distributions along the column. Other comparisons between single- and dual-frequency SRT results suggest that the use of the dual-frequency data often eliminates large overestimates in the PIA caused by anomalously low wind speeds in the outer swath. These low wind speeds result in a decrease in σ_R^0 that is attributed by the single-frequency algorithm to an increase in the PIA. With dual-frequency data, the decrease in the NRCS tends to occur at both frequencies so that the changes in $\delta\sigma_R^0$ are generally sensitive only to the differential path attenuation and relatively independent of variations in σ_R^0 with wind speed.

The final example shown here was measured on 13 September 2018 (orbit 25,808) over typhoon Florence situated to the east of the Philippine Islands. Because of the strong attenuation at Ka-band, the surface return (and near-surface rain return) is lost over several of the intense rain bands. Figure 9 shows the dual-frequency hybrid estimate of the Ku-band PIA on the left along with the reliability flags associated with the dual-frequency SRT and hybrid estimates. Although the hybrid estimate yields enhanced path attenuations in the inner eye wall and rain bands, the reliability flag images shown on the center and right indicate that for those regions in red, where RFlag $= 4$, the hybrid (and SRT) values underestimate the true PIA. Outside these regions, the dominant blue color shows that the estimates are considered generally accurate despite small areas of red-orange and green where the estimates are considered, respectively, unreliable or marginally reliable.

To compare these dual-frequency results to the Ku-band only estimates, we show in Fig. 10 the same set of plots except for a replacement of the dual-frequency estimates of Ku-band path attenuation by the single-frequency Ku-band estimates. Comparisons between the hybrid single- and dual-frequency Ku-band data (left-hand plots in Figs. 9, 10) show a significant increase in $A(Ku)$ in the eye wall and rain bands when only the Ku-band data are used. This enhancement is not surprising in that the loss of the Ka-band surface signal implies that the dual-frequency estimates are negatively biased. On the other hand, the SRT reliability flag plot in Fig. 10 (center) shows a significant degradation in quality relative to the dual-frequency result (center, Fig. 9). Nevertheless, the corresponding reliability flag image shows that the estimates are generally considered good in the areas of high path attenuation. Indeed, the Ku-band surface signal shows the data to be above the noise level throughout the area. Finally, a comparison of the reliability flag for $SRT(Ku)$ in Fig. 10, center, with that for hybrid (Ku) (right) indicates a significant improvement in going from $SRT(Ku)$ to hybrid (Ku). The reason for this improvement is that the HB at Ku-band is often more

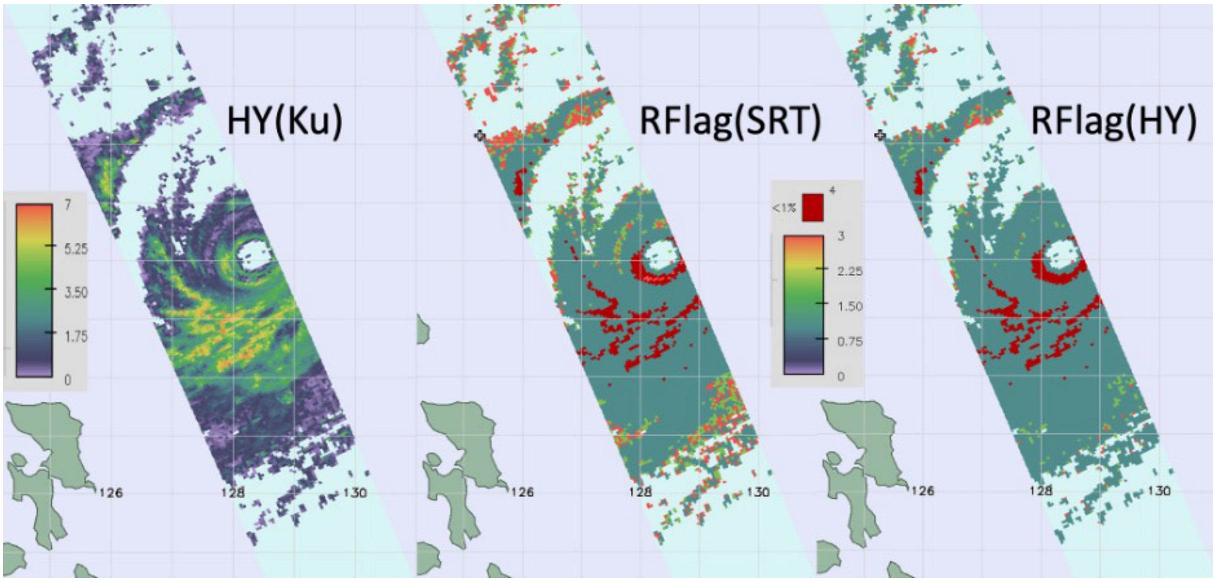

Fig. 9. Left: Path attenuation at Ku-band (dB) as estimated by the dual-frequency hybrid method; Center: Reliability flag for the SRT dual-frequency estimate of Ku-band path attenuation; Right: same as center plot but for the hybrid dual-frequency estimate of $A_\delta(Ku)$. In both center and right plots, areas in red give the locations where the Ka-band surface signal is lost.

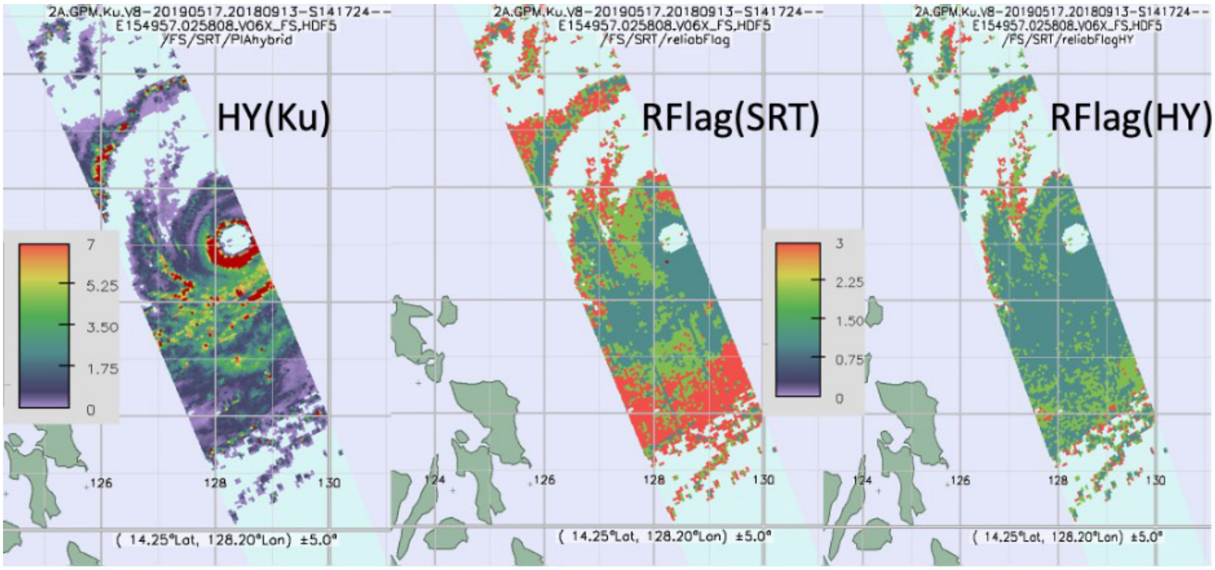

Fig. 10. Same as Fig. 9 but for the single-frequency Ku-band Hybrid and SRT methods.

accurate than the SRT, particularly in light to moderate rain rates, so that the weighted mean of the SRT and HB yields generally good estimates, although not as good as the dual-frequency hybrid (right, Fig. 9) outside the areas of high rain rate.

4. Statistics of the estimates

The examples in the previous section reveal some general characteristics of the hybrid and SRT estimates. First, the dual-frequency SRT estimates are generally more accurate than their single-frequency counterparts. An important exception to this rule occurs in high rain rate cases where the Ka-band surface signal is lost, i.e., the surface return is near or below the receiver noise.

When dual-frequency data exist, the SRT is fairly accurate so in going from the SRT to the hybrid, the improvement occurs primarily in the light rain rate areas where the HB and DW methods may be comparable to or more accurate than the SRT. As the variance of $\delta\sigma^0$ is relatively independent of incidence angle, apart from near-nadir incidence over land, the weightings also should be relatively independent of incidence angle. At near-nadir incidence over land, the increase in the standard deviation of $\delta\sigma^0$ will decrease the weight of the SRT and increase the weights of HB and DW in the hybrid estimate.

For single-frequency Ku-band operation, the situation changes. Most importantly, $SRT(Ku)$ often has large relative errors because the standard deviation of $\sigma^0(Ku)$ is generally large at high incidence angles over ocean and at near-nadir incidence over land. This implies that the HB, which is more accurate at Ku-band than at Ka-band, will tend to be weighted more highly than the $SRT(Ku)$, particularly at light to moderate rain rates where $\zeta(Ku)$ is small. For the single frequency Ka-band, the relative weights change because the mean Ka-band path attenuation increases by approximately a factor of 6 whereas the standard deviation of $\sigma^0(Ka)$ is nearly the same as that at Ku-band. For the HB, the mean and variance of $\zeta(Ka)$ are significantly larger than those of $\zeta(Ku)$ so that the error variance of $HB(Ka)$ increases relative to that of $HB(Ku)$. These changes imply that at Ka-band, the SRT weight will increase and the HB weight will decrease relative to the weights at Ku-band. Indeed, since the weights must sum to 1, and as only two single-frequency methods are considered (SRT and HB), an increase in the weight of one is directly linked to a decrease in the weight of the other.

Scatterplots (2D histograms) of path attenuations derived from single-frequency Ku-band data are shown in Fig. 11 using data from the entire month of September 2018. In these plots, only those data are plotted for which the SRT is considered reliable or marginally reliable. Data shown in the top set panels are taken from an incidence angle at the scan edge, -18^0, whereas the bottom set of panels are taken from an incidence angle at -3.75^0. Comparisons between SRT and hybrid (HY) generally show good agreement; however, there are a number of cases where SRT shows high overestimates whereas the hybrid estimates are small. The SRT overestimates are more common at the high incidence angle where low wind speeds in the presence of rain serve to decrease $\sigma^0(Ku)$ and lead to positive biases in the SRT PIA. These overestimates tend to be eliminated in the hybrid which relies on the HB in these cases. Comparisons between HB and hybrid and HB and SRT show good correlations at low values of path attenuation; at higher path attenuations, however, the HB underestimates relative to SRT and hybrid. These basic trends are repeated in the results from single-frequency Ka-band data (Fig. 12) except that the weighting of the SRT, relative to the HB, is stronger for Ka-band since the variance of SRT remains approximately the same as that at Ku-band whereas the variance of HB becomes higher because of the higher values of $\zeta(Ka)$.

These trends tend to remain the same when the ocean background is replaced by a land background. One interesting difference, however, is that a larger number of SRT overestimates occur at near-nadir angles and fewer overestimates at off-nadir angles. For the land cases, assuming that we accept only positive values of path attenuation, the large positive biases in the SRT occur because of the much larger SD of σ^0 at near-nadir angles.

Comparisons of the dual-frequency derived Ku-band PIA over ocean are shown in Fig. 13. Results from a near-nadir angle (-3.75^0) are shown on the left and at the scan edge (-18^0) on the right. As the SRT tends to dominate in these cases, the SRT versus hybrid results tend to be highly correlated but with some scatter at small values of the path attenuation where the HB and DW become more important. Generally good correlations are evident between HB and hybrid but with a fair amount of scatter about the 1:1 line. The DW results, which have a relatively small effect on the hybrid because of their fairly high variances, show positive bias relative to the hybrid for both incidence angles. The reason for this behavior appears to be the high variability in this estimate at light rain rates. In fact, the positive bias in the plots is misleading as the relatively large number of negative DW estimates are not shown in the plot. It should be noted that, except for a scaling factor, the path attenuation results at Ka-band, KaDF, are similar to those at Ku-band, KuDF, as a consequence of the fact that both are derived from the differential path attenuation estimate.

5. Discussion and summary

This paper has presented a summary of the current (V06X) path attenuation algorithm in the DPR opera-

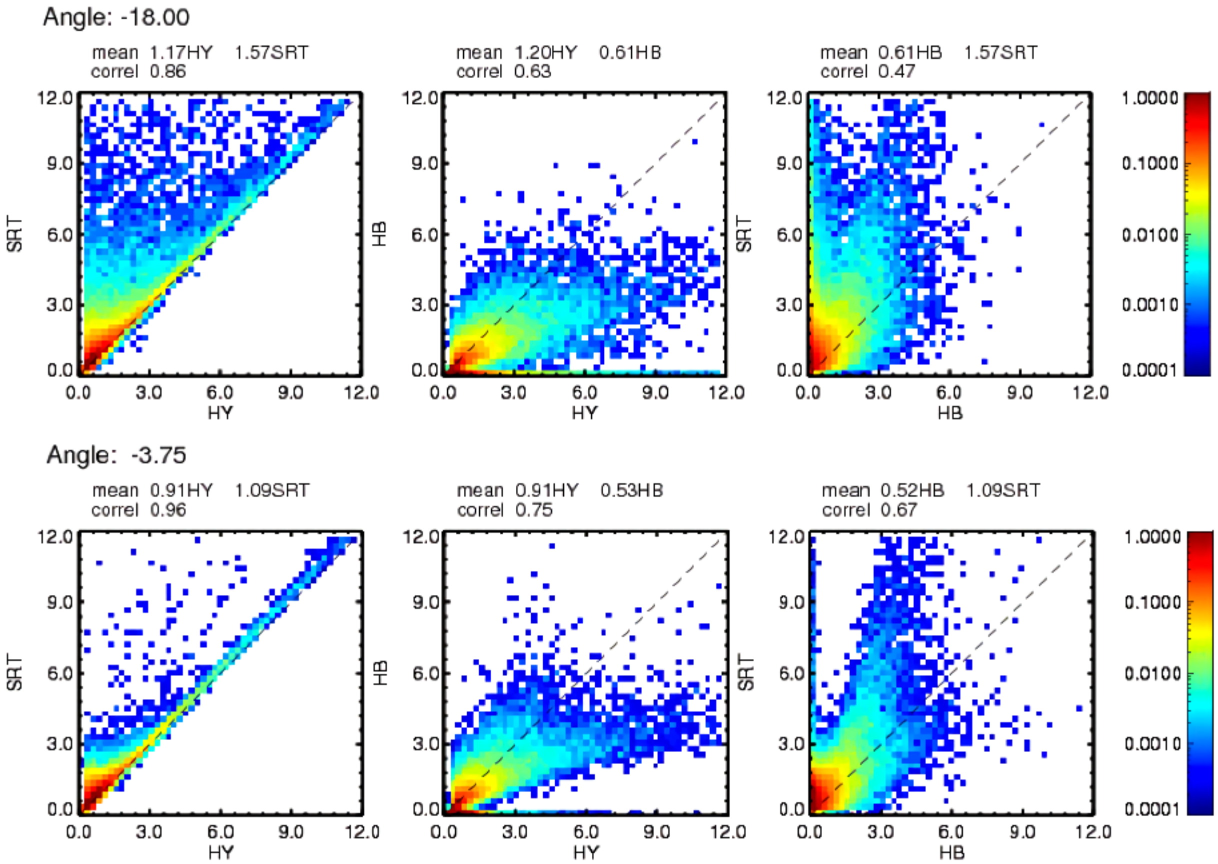

Fig. 11. Scatterplots of path attenuations in dB over ocean using SRT, HB and hybrid (HY) at Ku-band using single-frequency data from measurements of the DPR taken during September 2018. The set of 3 panels on the top are taken at incidence angle -18^0 while those on the bottom are taken at -3.75^0. Note that negative angles are taken from the left side of the swath as viewed by an observer looking in the direction of the satellite motion.

tional system. Both single- and dual-frequency versions of the SRT have been implemented as have the single- and dual-frequency versions of a hybrid estimate that combines SRT with HB and, in the case of dual-frequencies, with the DW method. The current code is able to operate on DPR data taken after May 2018 where dual-frequency data exist over the full swath.

The results indicate, with respect to the accuracy of the estimates, that the hybrid is to be preferred over the SRT and dual-frequency results over single-frequency. The dual-frequency estimates, however, normally require both Ku- and Ka-band precipitation and surface returns to be present and above the noise level. These conditions are not met at very light rain rates, where only the Ku-band precipitation signal is present, and at high rain rates where the surface and near-surface rain returns at Ka-band can be lost through attenuation. (As an aside we note that although the dual-frequency HB and DW methods cannot be applied in light rain conditions where the Ka-band rain return is absent, the dual-frequency SRT can be employed since the Ka-band surface signal in these cases will almost always be measurable. Of course, this information can only be used in correcting or constraining the Ku-band rain profile.) It is worth noting that the surface loss at Ka-band depends on incidence angle and surface type as the surface cross sections decrease with incidence angle which decreases the dynamic range of measurable path attenuations.

In comparing the hybrid and SRT estimates, note that the former is sensitive to the weighting of the component path attenuations: a change in any of the error models will modify the result. In particular, for the results presented, errors caused by sampling fluctuations have not been included. Their inclusion will increase the weight of the HB method and lessen

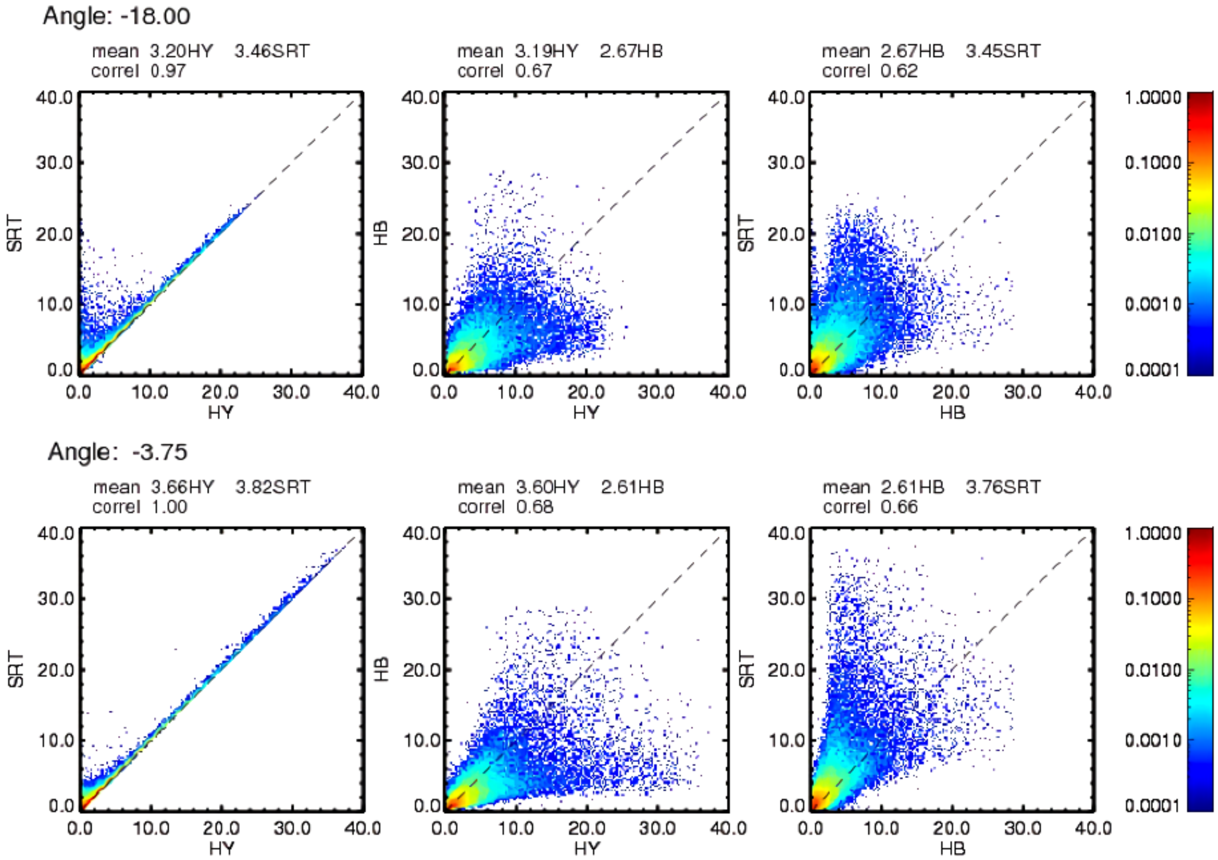

Fig. 12. Same as Fig. 11 except for the use of Ka-band single-frequency data rather than Ku-band data.

the weights of the SRT and DW as the influence of sampling errors on the HB is relatively minor whereas their impact on SRT and DW is more substantial.

Other errors in the methods are difficult to model because they depend on how well the predominant hydrometeor type can be distinguished as a function of radar range. The HB method, in particular, requires a knowledge of the dominant phase state as a function of radar range so that the appropriate α values can be inserted into (2). (Note that α is allowed to vary with range; that is, (1) and (2) provide solutions to the HB differential equation when α is range-dependent. A range-dependent β, however, does not satisfy the HB differential equation so that an error will be introduced if this parameter is allowed to vary with range.) This problem is fairly straightforward when a bright-band is detected where the mixed phase region can be used to separate snow above from rain below. The task is much more difficult in convective rain where the mixed phase region is not easily identifiable. In the present code, the parameter 'binNode' from the DSD module, derived from the GANAL data (Iguchi et al. 2018), is used in convective rain to estimate the top and bottom of the mixed phase region. In stratiform cases, the classification algorithm (Le and Chandrasekhar 2013; Awaka et al. 2009) provides the top and bottom of the mixed phase region. Of course, even when this region is accurately identified, the scattering properties in general and the *k-Z* relationship in particular, exhibit large variability. In the present code, results from the melting layer model described by Liao and Meneghini (2005) and Liao et al. (2009) have been used. Knowledge of the particle phase state with location along the radar column also affects the DW method. In particular, if snow is present in the near-surface gate at which the DW method is applied, then the estimate of DFR from Z_m, and the error model itself, will be incorrect as these results apply only to liquid hydrometeors. In the present code, the DW estimate is set to missing if the range gate just above the surface is judged to contain snow or mixed phase particles.

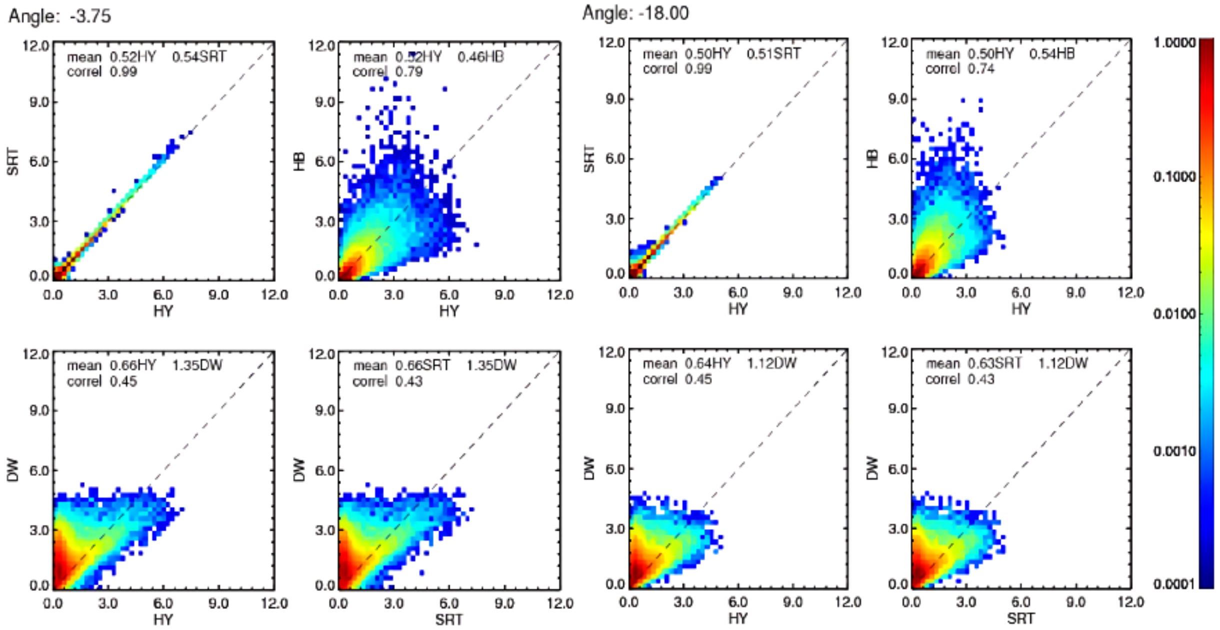

Fig. 13. Scatterplots of path attenuations at Ku-band in dB over ocean using dual-frequency data (KuDF) from measurements of the DPR taken during September 2018. Set of 4 panels on the left are taken at incidence angle -3.75^0 while those on right are taken at -18^0.

Another type of error arises from the need to compare PIA estimates down to the surface; this requires an assumption in the HB and DW techniques regarding the behavior of Z_m between the last clutter-free range gate and the surface. Clearly, this task becomes more prone to error as the incidence angle increases where the distance between the surface and the lowest clutter-free gate becomes larger. The errors can be severe for the DW method as the estimate of DFR_m (20) depends entirely on the $Z_m(Ku)$, $Z_m(Ka)$ values at the near-surface gate. Because of the sensitivity of the method to the extrapolation that is used, the DW results in this paper are derived from the last clutter-free gate rather than the extrapolated values to the surface. For the HB, a simple linear interpolation is used based on the five clutter-free values of Z_m closest to the surface; however, if the slope of this line is positive (increasing toward the surface) and greater than some threshold value, Z_m is assumed to be constant in this lowest segment of the profile.

The non-uniform beamfilling (NUBF) problem has not been mentioned in the paper but can result in severe underestimates of the PIA by the SRT (Nakamura 1991; Durden et al. 1998; Kozu and Iguchi 1999; Takahashi et al. 2005; Durden and Tanelli 2008; Short et al. 2015). As the HB and the DW are less affected by NUBF, relating differences among the PIA estimates to the non-uniformity of rain might prove useful. Another scattering mechanism that has not been considered is multiple scattering (Battaglia et al. 2015). This occurs much more frequently at Ka-band than at Ku-band and will render any Ka-band or dual-frequency based estimate of the rain profile unreliable. On the other hand, if the surface is detected and the magnitude of the return is much larger than the nearby returns, then it is hypothesized that the surface return is indicative of the single-scattering path attenuation and can be used to estimate a path-integrated rain rate. This hypothesis, however, requires testing. One other long-standing problem with the SRT over ocean is the influence of the raindrop splash effect on the normalized surface cross section. This is a formidable problem as the influence of the splash effect on the NRCS depends on wind speed and direction, radar frequency, incidence angle and rainfall rate (Contreras and Plant 2006). Over land, surface wetting and changes in soil moisture can lead to differences in the NRCS outside and within the rain (Seto and Iguchi 2007).

As a final comment, we note that the hybrid estimates presented here have been separated into single- and dual-frequency types. What may be needed in version 7 of the algorithm, apart from a review of the error variance models and the inclusion of sampling errors, is a Ku-band hybrid estimate which combines the two and which reduces to the single-frequency Ku-band result when the Ka-band signal is unavailable either because of limited detection in light rain or signal loss in heavy rain. The Ka-band PIA estimate in these cases would take the form of a simple scaling of the Ku-band estimate, e.g., $A(Ka) = 6A(Ku)$.

References

Adirosi, E., L. Baldini, N. Roberto, P. Gatlin, and A. Tokay, 2016: Improvement of vertical profiles of raindrop size distribution from micro rain radar using 2D video disdrometer measurements. *Atmos. Res.*, **169**, 404–415.

Awaka, J., T. Iguchi, and K. Okamoto, 2009: TRMM PR standard algorithm 2A23 and its performance on bright band detection. *J. Meteor. Soc. Japan*, **87A**, 31–52.

Battaglia, A., S. Tanelli, K. Mroz, and F. Tridon, 2015: Multiple scattering in observations of the GPM dual-frequency precipitation radar: Evidence and impact on retrievals. *J. Geophys. Res: Atmos.*, **120**, 4090–4101.

Contreras, R. F., and W. J. Plant, 2006: Surface effect of rain on microwave backscatter from the ocean: Measurements and modelling. *J. Geophys. Res.*, **111**, C08019, doi:1029/2005JC003356.

Daley, R., 1991: *Atmospheric Data Analysis*. Cambridge University Press, 457 pp.

Durden, S. L., 2018: Relating GPM radar reflectivity profile characteristics to path-integrated attenuation. *IEEE Trans. GeoSci. Remote Sens.*, **57**, 4065–4074.

Durden, S. L., and S. Tanelli, 2008: Predicted effects of nonuniform beam filling on GPM radar data. *IEEE Geosci. Remote Sens. Lett.*, **5**, 308–310.

Durden, S. L., Z. S. Haddad, A. Kitiyakara, and F. K. Li, 1998: Effects of nonuniform beam filling on rainfall retrieval for the TRMM Precipitation Radar. *J. Atmos. Oceanic Technol.*, **15**, 635–646.

Durden, S. L., L. Li, E. Im, and S. H. Yueh, 2003: A surface reference technique for airborne Doppler radar measurements in hurricanes. *J. Atmos. Oceanic Technol.*, **20**, 269–275.

Eccles, P. J., and E. A. Mueller, 1971: X-band attenuation and liquid water content estimation by a dual-wavelength radar. *J. Appl. Meteor.*, **10**, 1252–1259.

Hitschfeld, W., and J. Bordan, 1954: Errors inherent in the radar measurement of rainfall at attenuating wavelengths. *J. Meteor.*, **11**, 58–67.

Iguchi, T., and R. Meneghini, 1994: Intercomparison of single-frequency methods for retrieving a vertical rain profile from airborne or spaceborne radar data. *J. Atmos. Oceanic Technol.*, **11**, 1507–1516.

Iguchi, T., T. Kozu, R. Meneghini, J. Awaka, and K. Okamoto, 2000: Rain profiling algorithm for the TRMM Precipitation Radar. *J. Appl. Meteor.*, **39**, 2038–2052.

Iguchi, T., T. Kozu, J. Kwiatkowski, R. Meneghini, J. Awaka, and K. Okamoto, 2009: Uncertainties in the rain profiling algorithm for the TRMM Precipitation Radar. *J. Meteor. Soc. Japan*, **87A**, 1–30.

Iguchi, T., S. Seto, R. Meneghini, N. Yoshida, J. Awaka, M. Le, V. Chandrasekar, and T. Kubota, 2018: *GPM/DPR level-2 algorithm theoretical basis document*. JAXA–NASA Tech. Rep., 81 pp. [Available at http://www.eorc.jaxa.jp/GPM/doc/algorithm/ATBD_DPR_201708_whole_1.pdf.]

Kozu, T., and T. Iguchi, 1999: Nonuniform beamfilling correction for spaceborne radar rainfall measurement: Implications from TOGA COARE Radar data analysis. *J. Atmos. Oceanic Technol.*, **16**, 1722–1735.

Le, M., and V. Chandrasekar, 2013: Hydrometeor profile characterization method for dual-frequency precipitation radar onboard the GPM. *IEEE Trans. Geosci. Remote Sens.*, **51**, 3648–3658.

Li, L., E. Im, S. L. Durden, and Z. S. Haddad, 2002: A surface wind model-based method to estimate rain-induced radar path attenuation over ocean. *J. Atmos. Oceanic Technol.*, **19**, 658–672.

Li, L., E. Im, L. N. Connor, and P. S. Chang, 2004: Retrieving ocean surface wind speed from the TRMM Precipitation Radar measurements. *IEEE Trans. Geosci. Remote Sens.*, **42**, 1271–1282.

Liao, L., and R. Meneghini, 2005: On modeling air/spaceborne radar returns in the melting layer. *IEEE Geosci. Remote Sens.*, **43**, 2799–2809.

Liao, L., and R. Meneghini, 2019: Physical evaluation of GPM DPR single- and dual-wavelength algorithms. *J. Atmos. Oceanic Technol.*, **36**, 883–902.

Liao, L., R. Meneghini, L. Tian, and G. M. Heymsfield, 2009: Measurements and simulations of nadir-viewing radar returns from the melting layer at X- and W-bands. *J. Appl. Meteor. Climatol.*, **48**, 2215–2226.

Meneghini, R., J. Eckerman, and D. Atlas, 1983: Determination of rain rate from a spaceborne radar using measurements of total attenuation. *IEEE Trans. Geosci. Remote Sens.*, **GE-21**, 34–43.

Meneghini, R., T. Kozu, H. Kumagai, and W. C. Boncyk, 1992: A study of rain estimation methods from space using dual-wavelength radar measurements at near-nadir incidence over ocean. *J. Atmos. Oceanic Technol.*, **9**, 364–382.

Meneghini, R., T. Iguchi, T. Kozu, L. Liao, K. Okamoto, J. A. Jones, and J. Kwiatkowski, 2000: Use of the surface reference technique for path attenuation estimates form the TRMM Precipitation Radar. *J. Appl. Meteor.*, **39**, 2053–2070.

Meneghini, R., J. A. Jones, T. Iguchi, K. Okamoto, and J. Kwiatkowski, 2004: A hybrid surface reference technique and its application to the TRMM Precipitation Radar. *J. Atmos. Oceanic Technol.*, **21**, 1645-1658.

Meneghini, R., L. Liao, S. Tanelli, and S. L. Durden, 2012:

Assessment of the performance of a dual-frequency surface reference technique over ocean. *IEEE Trans. Geosci. Remote Sens.*, **50**, 2968–2977.

Meneghini, R., H. Kim, L. Liao, J. Jones, and J. M. Kwiatkowski, 2015: An initial assessment of the surface reference technique applied to data from the dual-frequency precipitation radar (DPR) on the GPM satellite. *J. Atmos. Oceanic Technol.*, **32**, 2281–2296.

Nakamura, K., 1991: Biases of rain retrieval algorithms for spaceborne radar caused by nonuniformity of rain. *J. Atmos. Oceanic Technol.*, **8**, 363–373.

Seto, S., and T. Iguchi, 2007: Rainfall-induced changes in actual surface backscattering cross sections and effects on rain-rate estimates by spaceborne Precipitation Radar. *J. Atmos. Oceanic Technol.*, **24**, 1693–1709.

Seto, S., and T. Iguchi, 2015: Intercomparison of attenuation correction methods for the GPM dual-frequency precipitation radar. *J. Atmos. Oceanic Technol.*, **32**, 915–926.

Seto, S., T. Iguchi, and T. Oki, 2013: The basic performance of a precipitation retrieval algorithm for the Global Precipitation Measurement mission's single/dual frequency radar measurements. *IEEE Trans. Geosci. Remote Sens.*, **51**, 5239–5251.

Seto, S., T. Shimozuma, T. Iguchi, and T. Kozu, 2016: Spatial and temporal variations of mass-weighted mean diameter estimated by GPM/DPR. *2016 IEEE International Geoscience and Remote Sensing Symposium (IGARSS)*, Beijing, 3938–3940.

Seto, S., T. Iguchi, R. Meneghini, J. Awaka, T. Kubota, T. Masaki, and N. Takahashi, 2020: The precipitation rate retrieval algorithms for the GPM Dual-frequency Precipitation Radar. *J. Meteor. Soc. Japan*, accepted.

Short, D. A., R. Meneghini, A. E. Emory, and M. R. Schwaller, 2015: Reduction of nonuniform beamfilling effects by multiple constraints: A simulation study. *J. Atmos. Oceanic Technol.*, **32**, 2114–2124.

Takahashi, N., H. Hanado, and T. Iguchi, 2005: Estimation of path-integrated attenuation and its nonuniformity from TRMM/PR range profile data. *IEEE. Trans. Geosci. Remote Sens.*, **44**, 3276–3283.

Tanelli, S., S. L. Durden, and E. Im, 2006: Simultaneous measurements of Ku- and Ka-band sea surface cross sections by an airborne radar. *IEEE Geosci. Remote Sens. Lett.*, **3**, 359–363.